New Phytologist

Research

Pore constrictions in intervessel pit membranes provide a mechanistic explanation for xylem embolism resistance in angiosperms

Lucian Kaack[1]*, Matthias Weber[2]*, Emilie Isasa[3], Zohreh Karimi[4], Shan Li[5], Luciano Pereira[1], Christophe L. Trabi[1], Ya Zhang[6], H. Jochen Schenk[7], Bernhard Schuldt[3], Volker Schmidt[2] and Steven Jansen[1]

[1]Institute of Systematic Botany and Ecology, Ulm University, Albert-Einstein-Allee 11, Ulm D-89081, Germany; [2]Institute of Stochastics, Ulm University, Helmholtzstraße 18, Ulm D-89069, Germany; [3]Ecophysiology and Vegetation Ecology, Julius-von-Sachs-Institute for Biological Sciences, University of Würzburg, Julius-von-Sachs-Platz 3 Würzburg D-97082, Germany; [4]Department of Biology, Faculty of Sciences, Golestan University, Shahid Beheshti St., Gorgan 15759-49138, Iran; [5]Department of Wood Anatomy and Utilization, Research Institute of Wood Industry, Chinese Academy of Forestry, Beijing 100091, China; [6]College of Life Sciences, Anhui Normal University, Beijingdong Road 1, Wuhu 241000, China; [7]Department of Biological Science, California State University Fullerton, Fullerton, CA 92834-6850, USA

Author for correspondence:
Lucian Kaack
Email: lucian.kaack@uni-ulm.de

Received: *16 October 2020*
Accepted: *9 February 2021*

New Phytologist (2021) **230:** 1829–1843
doi: 10.1111/nph.17282

Key words: angiosperm xylem, embolism, embolism propagation, pit membrane, pore constriction, porous medium, ultrastructural modelling, vessel.

Summary

- Embolism spreading in angiosperm xylem occurs via mesoporous pit membranes between vessels. Here, we investigate how the size of pore constrictions in pit membranes is related to pit membrane thickness and embolism resistance.
- Pit membranes were modelled as multiple layers to investigate how pit membrane thickness and the number of intervessel pits per vessel determine pore constriction sizes, the probability of encountering large pores, and embolism resistance. These estimations were complemented by measurements of pit membrane thickness, embolism resistance, and number of intervessel pits per vessel in stem xylem (n = 31, 31 and 20 species, respectively).
- The modelled constriction sizes in pit membranes decreased with increasing membrane thickness, explaining the measured relationship between pit membrane thickness and embolism resistance. The number of pits per vessel affected constriction size and embolism resistance much less than pit membrane thickness. Moreover, a strong relationship between modelled and measured embolism resistance was observed.
- Pore constrictions provide a mechanistic explanation for why pit membrane thickness determines embolism resistance, which suggests that hydraulic safety can be uncoupled from hydraulic efficiency. Although embolism spreading remains puzzling and encompasses more than pore constriction sizes, angiosperms are unlikely to have leaky pit membranes, which enables tensile transport of water.

Introduction

Xylem sap in vessel-bearing angiosperms crosses numerous intervessel walls from the root to the leaf xylem, depending on the plant size, vessel length, intervessel connectivity, and vessel network topology (Loepfe *et al.*, 2007). It is well known that small openings in the secondary cell wall, which are described as bordered pits, play an important role in hydraulic transport between adjacent vessels, and also in failure of the transport system by gas entry (i.e. embolism) (Choat *et al.*, 2008; Kaack *et al.*, 2019). Since water transport efficiency is tightly related to transpiration and photosynthesis, drought-induced embolism formation can have major implications for plant performance, especially under drought (Li *et al.*, 2016a,b; Sorek *et al.*, 2021). Yet many details about the mechanistic relationship between embolism formation and the anatomical determinants of pits remain unclear.

An angiosperm vessel is estimated to have a median of *c.* 14 188 intervessel pits, with values for different species varying > 200-fold, from *c.* 500 pits to > 100 000 (sample size, n = 72 species; Supporting Information Fig. S1, based on data from the literature). Each bordered pit pair has a pit membrane, which is mainly composed of *c.* 20 nm wide cellulose microfibril aggregates. These pit membranes develop from the primary cell wall and middle lamella, and have a mean diameter of 4.8 ± 2.4 μm (n = 43 species; Jansen *et al.*, 2009, 2011). Before pit membranes become hydraulically functional, hemicellulose and pectin compounds are enzymatically removed (O'Brien, 1970; Herbette *et al.*, 2015; Klepsch *et al.*, 2016). Therefore, fully mature pit

*These authors contributed equally to this work.

membranes are nonwoven, fibrous porous media of mainly cellulose, with a thickness between *c.* 160 nm and 1000 nm (Esau, 1977; Pesacreta *et al.*, 2005; Kaack *et al.*, 2019).

Pit membranes control the immediate entry of gas from neighbouring, embolised conduits, and may become sites of further embolism propagation under persistent drought (Zimmermann, 1983; Brodersen *et al.*, 2013; Brodribb *et al.*, 2016; Choat *et al.*, 2016; Roth-Nebelsick, 2019). Embolism spreading from an embolised vessel to a sap-filled vessel has been described as 'air-seeding', but the actual mechanism underlying embolism formation represents one of the major knowledge gaps in our understanding of water transport in plants (Jansen *et al.*, 2018). It is assumed that propagation of drought-induced embolism from one vessel to a neighbouring vessel is affected, among other factors, by pore dimensions of intervessel pit membranes. Here, we use the broader term 'embolism spreading' or 'propagation' instead of 'air-seeding' because embolism spreading includes both mass flow and diffusion of gas across pit membranes. Air-seeding, however, is limited to mass flow only, and embolism formation may not be caused only by mass flow of gas (Guan *et al.*, 2021). Also, 'embolism' is used instead of the term 'cavitation', because the triggering process leading to embolism is unlikely to be due to the formation of a void by phase transition from liquid to gas, but most likely caused by pre-existing bubbles (Hölttä *et al.*, 2002; Schenk *et al.*, 2017).

Instead of perfectly flat, two-dimensional structures, pit membranes are porous media, with pores that include multiple constrictions, with the respective narrowest constriction in each pore governing the flow of water and gas and, consequently, embolism spreading (Fig. 1; Kaack *et al.*, 2019). Estimates of bottleneck diameters (i.e. constriction sizes) vary from 5 nm to well above 200 nm (Choat *et al.*, 2003; Sano, 2005; Jansen *et al.*, 2009; Hillabrand *et al.*, 2016). Part of this variation is caused by sample preparation for imaging by scanning electron microscopy (SEM), which induces a reduction in the pit membrane thickness (T_{PM}) of up to 50% during drying, with frequently enlarged pores and cracks (Shane *et al.*, 2000; Jansen *et al.*, 2008; Zhang *et al.*, 2017). Moreover, the challenge is to quantify the size and shape of pit membrane pores using a three-dimensional approach. A three-dimensional model based on data obtained from transmission electron microscopy (TEM) of fresh and shrunken pit membranes indicated a high porosity (i.e. void volume fraction) of 81%, highly interconnected pores with nontortuous, unbending passageways, a lack of dead-end pores, and the occurrence of multiple pore constrictions within a single pore (Zhang *et al.*, 2020). Based on a shrinkage model and gold perfusion experiments, it has been found that constriction sizes in pit membrane pores vary from 5 to < 50 nm, with an average diameter of *c.* 20 nm (Choat *et al.*, 2003, 2004; Zhang *et al.*, 2020). The evidence available suggests that pore sizes are fairly constant for angiosperm species, despite considerable variation in T_{PM}. Indeed, pore constriction sizes of *c.* 20 nm are found both in species with thin (*c.* 200 nm) pit membranes and those with thick (> 500 nm) pit membranes (Fig. S2), and there is no evidence for large (> 50 nm) pore size differences among species (Zhang *et al.*, 2020). However, Zhang *et al.* (2020) who conducted experiments using gold particles, recorded only the sizes of the particles that were able to penetrate pit membranes, but did not quantitatively report the penetration depth or the frequency distribution of particle sizes. Could small differences in pore constriction sizes and frequencies in pit membranes explain the relatively variable xylem embolism resistances within angiosperms (Choat *et al.*, 2012)?

Angiosperm species with thick pit membranes were found to be more resistant to drought-induced embolism than species with thin pit membranes (Jansen *et al.*, 2009; Li *et al.*, 2016a,b; Dória *et al.*, 2019; Trueba *et al.*, 2019; Thonglim *et al.*, 2020; Levionnois *et al.*, 2021). This functional link between T_{PM} and P_{50}, which is the xylem water potential corresponding to a 50% loss in maximum hydraulic conductivity (P_{50}, MPa), is valid at the interspecific (Li *et al.*, 2016a,b), intrageneric (Lens *et al.*, 2011; Plavcová & Hacke, 2012; Scholz *et al.*, 2013) and intraspecific level (Schuldt *et al.*, 2016). Variation in T_{PM} is mainly determined by the number of microfibril layers, with thin pit membranes consisting of fewer microfibril layers than thick pit membranes. Note that the number of layers can be estimated by assuming that cellulose fibres have a diameter of *c.* 20 nm (Pesacreta *et al.*, 2005), and 20 nm pore spaces between each layer based on gold perfusion experiments (Table 1; Zhang *et al.*, 2020). As such, pit membranes with a thickness between 140 and 1180 nm (Jansen *et al.*, 2009; Li *et al.*, 2016a,b) include between 4 and 30 layers. In our models, bottlenecks in a given pore are formed by the pore constrictions between cellulose fibres within a single layer. Therefore, the number of constrictions within a pore (N_C) equals the number of layers (Table 1). Since it is unknown why thin pit membranes are more vulnerable to embolism than thick pit membranes (Jansen *et al.*, 2018), we explore the hypothesis that the likelihood of leaky pores with wide pore constrictions is affected by T_{PM}, which could explain why T_{PM} is related to P_{50}.

The mismatch between pore size estimations based on colloidal gold perfusion and experimental values of embolism resistance resulted in the hypothesis that a very small percentage of pit membranes might contain large pores (Choat *et al.*, 2003, 2004). These rare pit membrane pores are assumed to cause low embolism resistance. The idea of such leaky, rare pits was further enhanced when variation in P_{50} at an interspecific level was found to decrease with increasing pit membrane surface area in intervessel walls (Wheeler *et al.*, 2005). The 'pit area hypothesis' (Sperry *et al.*, 2006), which was later termed 'rare pit hypothesis', provided a possible explanation for high vulnerability to embolism, and relied on a largely two-dimensional interpretation of pit membranes (Hacke *et al.*, 2007; Christman *et al.*, 2009, 2012; Plavcová *et al.*, 2013). While the rare pit hypothesis follows a plausible mechanism that seems well supported by indirect evidence, it cannot be tested because the existence of a rare pit with a large pore cannot be observed directly, and it is impossible to verify from a statistical point of view. However, a three-dimensional modelling approach to estimating the likelihood of leaky pits is clearly lacking.

The number of layers in a pit membrane may affect the size of the narrowest constriction within a pore that crosses the entire

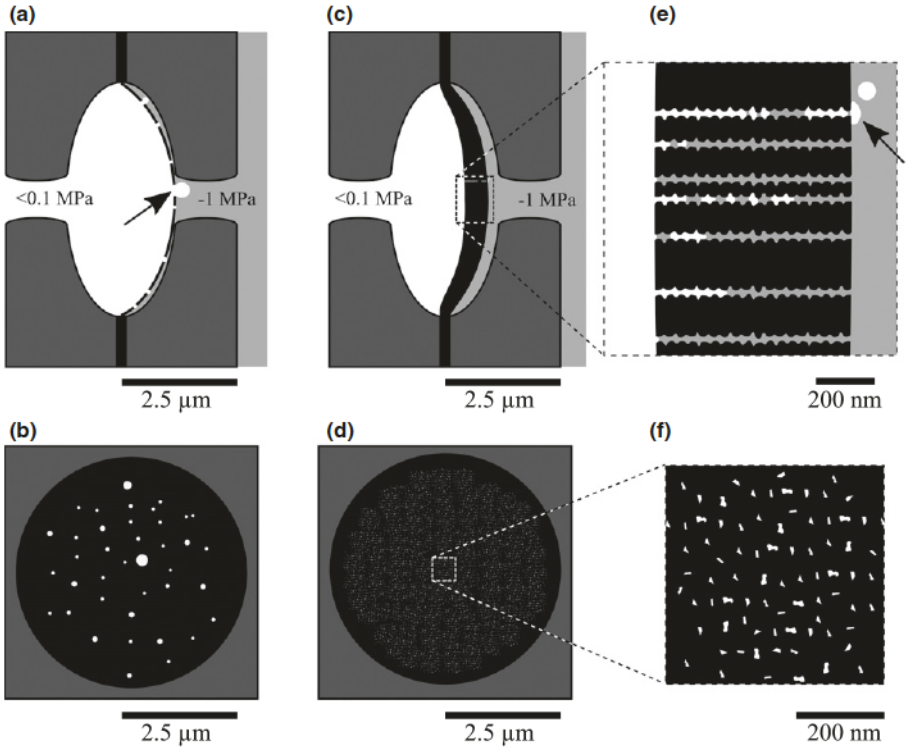

Fig. 1 Drawings illustrating a mainly two-dimensional (a, b) and three-dimensional (c, d, e, f) concept of angiosperm pit membranes and embolism spreading under aspiration. The upper images (a, c, e) show longitudinal views, while the lower images (b, d, f) represent frontal views. Large, cylindrical pores with circular cross-sections that are situated in a pit membrane with no defined thickness, in which the largest pore triggers air-seeding (arrows in (a) and (e)), or with a particular thickness and a three-dimensional concept of embolism propagation (c, e). Pores in a 670 nm thick pit membrane that is composed of multiple layers of cellulose fibrillar aggregates show multiple pore constrictions, which greatly reduces the size of the narrowest constriction within a pore (c, f). A magnified view is shown in (e) and (f), with seven hypothetical pores illustrating some of the shortest hydraulic paths (e), and with 18 pore constrictions per pore pathway (f). White areas represent gas, light grey areas represent xylem sap, black areas represent the solid phase of the primary cell wall, middle lamella or pit membrane, and dark grey areas represent the secondary cell wall.

Table 1 Overview of pit membrane thickness values (T_{PM}, nm) and their corresponding numbers of microfibril layers (N_L) according to the shrinkage model of Zhang *et al*. (2020).

T_{PM} (nm)	140	300	460	620	780	940	1100	1260
N_L	4	8	12	16	20	24	28	32

Assuming a homogeneous distribution of cellulose fibres, which have a diameter of 20 nm and a distance of 20 nm from each other, the number of pit membrane layers = (T_{PM} + 20)/40.

intervessel pit membrane. If embolism propagation is at least to some extent determined by the radius of a pore, the most important dimension of a pore is its minimum diameter, that is, the diameter of the narrowest bottleneck along the pore (R_{MIN}, nm). We can think of this diameter as the 'effective diameter' of the pore. The entry of an air–water meniscus or a bubble in a pit membrane is determined by the pore with the largest effective diameter within the pit membrane. Thus, embolism spreading and the minimum hydraulic resistance at the intervessel level are governed by the pore with the largest effective diameter in all pit membranes of a single vessel.

First, we hypothesise that the effective diameter of each pore becomes smaller with increasing T_{PM} and number of pit membrane layers, as proposed by Kaack *et al.* (2019) (Hypothesis 1). This hypothesis is investigated at the individual pit membrane level based on a stochastic pit membrane model. Second, we hypothesise that model-based values of embolism spreading largely agree with embolism resistance measurements for a large number of species (Hypothesis 2). Third, we expect that the probability of having a leaky pit membrane is low at the whole vessel level, and is affected by both T_{PM} (Li *et al.*, 2016a,b) and the total number of intervessel pits per vessel (N_{PIT}; Hypothesis 3) (Wheeler *et al.*, 2005). The second hypothesis is tested based on experimental data on embolism resistance and anatomical measurements, while two further stochastic pit membrane models are developed to test the third hypothesis. Testing these hypotheses should help us to better understand the functional link between embolism resistance and pit membrane ultrastructure.

Materials and Methods

Pit membrane modelling

To better understand the relationship between T_{PM} and embolism resistance, we developed three complementary pit membrane models. For reasons of simplicity, we assumed the existence of more-or-less cylindrical pores, which govern

transport phenomena, and modelled each pore as a three-dimensional object instead of a circular, flat opening (Sperry & Hacke, 2004; Mrad *et al.*, 2018). Following the multi-layered pit membrane model of Zhang *et al.* (2020), we assumed that each pore penetrates a fixed number of microfibril layers. Each of these layers induces a pore constriction of some random radius (Fig. 1e). An important property of each pore is its effective radius, that is, the radius of the narrowest pore constriction within the entire pore (R_{MIN}, nm). We were especially interested in how R_{MIN} was affected by T_{PM} (Hypothesis 1), how modelled embolism resistance based on pore constriction size related to measured embolism resistance (Hypothesis 2), and to what extent the likelihood of leaky pit membranes at the entire vessel level was affected by T_{PM} and/or N_{PIT} (Hypothesis 3).

We developed a first model to estimate pit membrane leakiness at the structural level of a single pit membrane, and two models estimating leakiness at the vessel level. Detailed model descriptions and implementations are provided in Methods S1, S2 and S3.

Model 1. Pore constrictions in single intervessel pit membranes

In this model (Fig. 2a), we assumed circular pit membranes with a diameter of 5 µm (estimated from $n = 43$ species, based on Jansen *et al.*, 2009, 2011), each comprising a fixed number of pores, which were defined by a fixed number of pore constrictions. The random radius of each pore constriction was modelled by applying left-truncated normal distributions around mean constriction sizes of 20 nm (Scenario 1) and 100 nm (Scenario 2) in diameter to obtain an upper bound for the number of pores that fit into the membrane, resulting in 12 000 and 1100 pores, respectively.

For T_{PM} values between 140 and 1340 nm, we simulated random diameters of pore constrictions of a whole pit membrane and estimated the probability of encountering at least one pore larger than 35 nm (Scenario 1) or 180 nm (Scenario 2) in a pit membrane, as well as the mean and maximum constriction sizes (R_{MIN_mean}, R_{MIN_max}) of the effective radii R_{MIN}. R_{MIN_mean} and R_{MIN_max} were compared to the experimental data on embolism resistance with calculated embolism propagation pressures based on a modified Young–Laplace equation.

Model 2. Leaky pit membranes without hole alignment at the vessel level

Model 2 investigated the occurrence of leaky pit membranes at the vessel level (Fig. 2b) for T_{PM} values between 50 and 1200 nm and N_{PIT} values up to 400 000. Upper bounds for the probability of encountering at least one large pore, spanning an entire intervessel pit membrane with an effective radius larger than t, were calculated based on the probability P of encountering a large hole in any given layer (P^{N_L}) for $P = 0.25$ (Scenario 1) and $P = 0.50$ (Scenario 2). A large pore through the pit membrane was assumed to exist if there was at least one large hole in each layer. At the entire vessel level, the upper bound for the probability of encountering a leaky pit membrane (P_{LP}) was given by:

$$P_{LP} = 1 - (1 - P^{N_L})^{N_{PIT}} \quad \text{Eqn 1}$$

Values of N_{PIT} ranging from 510 to 370 755, with a median value of 14 188, were calculated by dividing the total pit membrane surface area per vessel (A_P) by the corresponding bordered pit area for 72 species using our original data and data from the literature (Fig. S1; Wheeler *et al.*, 2005; Jansen *et al.*, 2011; Lens *et al.*, 2011; Nardini *et al.*, 2012; Scholz *et al.*, 2013; Klepsch *et al.*, 2016).

Model 3. Leaky pit membranes with hole alignment at the vessel level

Model 3 considered the alignment of holes within successive layers by modelling pit membranes as stacks of circular cellulose layers (based on T_{PM}). The pit membranes had a diameter of 5 µm, and each layer was perforated by a fixed number of holes (five in Scenario 1, and 10 in Scenario 2). The holes were randomly

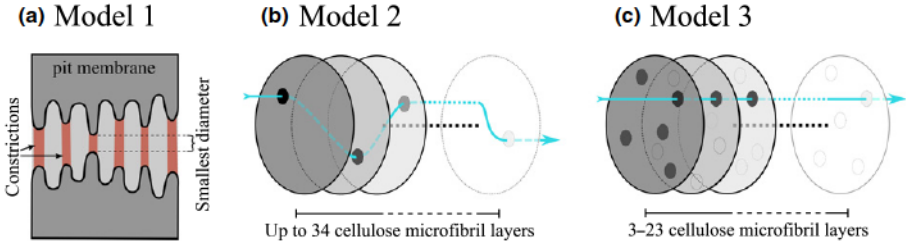

Fig. 2 Three mathematical models to investigate the functional link between pit membrane thickness and effective pore diameters. Model 1 (a) is based on a random number model to estimate the size of the narrowest constrictions of pores that traverse an entire pit membrane. This model is run 10 times following Scenario 1 and Scenario 2, which has small or large pore constrictions for 12 000 or 1100 pores per pit membrane, respectively, and with 4–34 constrictions per pore in 140–1350 nm thick pit membranes. Model 2 (b) examines the probability of large pores in 3000–400 000 intervessel pit membranes within an entire vessel. Pit membranes include up to 34 microfibril layers, assuming either a 0.25 or 0.5 chance of encountering a large hole in a single layer. This model is independent of the actual size of what we consider a large pore, and it does not incorporate alignment of pore constrictions. Model 3 (c) evaluates the probability of encountering pores with a large effective radius at the vessel level (i.e. for 30 000 intervessel pits), with pit membranes consisting of 3–23 microfibril layers, assuming 5 or 10 holes of 200 nm per layer. Alignment of holes was included in Model 3 by simulating random locations of holes in each pit microfibril layer, and requiring minimal overlap between consecutive holes to create a pore. Different shades of grey represent various microfibril layers, and a hypothetical flow path is indicated by the blue lines in (b) and (c).

located in each layer and had radii $t \geq 100$ nm. The locations of holes within and across layers were simulated stepwise and repeated 10^6 times for pit membranes with 3 to 23 layers (corresponding to T_{PM} values of 100–900 nm; Table 1). A pore only traversed all layers if there existed a sequence of holes that were aligned for each pair of adjacent layers (Fig. 2c). For each scenario, we estimated the probability that at least one hole with $t \geq 100$ nm crossed an entire pit membrane and the probability of encountering one large pore in a vessel with 30 000 intervessel pits. Minimal overlap of holes between adjacent layers was assumed to be sufficient for embolism spreading, even if only their edges were overlapping.

Experimental work

The three models were complemented by experimental data on embolism resistance ($n = 31$ species), T_{PM} measurements at the centre (T_{PM_centre}) and near the edges (T_{PM_edge}) ($n = 31$ species), and the total intervessel pit membrane area per average vessel (A_P, $n = 20$ species). The methods applied to obtain these data included well-established, previously published protocols (Wheeler *et al.*, 2005; Sperry *et al.*, 2006; Schuldt *et al.* 2016; Kotowska *et al.*, 2020; Zhang *et al.*, 2020), and they are described in detail in Methods S4. All data included original measurements, except for data retrieved from the literature for embolism resistance for five species, and for A_p values for four species.

Statistics and data processing

Data processing, simulations and statistical analyses were performed using Excel, R and Matlab. Shapiro–Wilk Tests were applied to test for normal distribution. Pearson's correlation coefficient was used to test for linear correlation. Basic linear and nonlinear regressions were fitted to test whether P_{12}, P_{50}, P_{88} (Table 2), and the slope of vulnerability curves were related to T_{PM} or A_P, and could be estimated. For each of the 31 species studied, we estimated embolism resistance by integrating their modelled R_{MIN_mean} and R_{MIN_max}, based on T_{PM}, into the equations for the relationship between T_{PM} and embolism propagation pressure used in Model 1 (Methods S5). This approach allowed us to compare estimated embolism propagation with experimental values of P_{12} and P_{50}.

Results

How likely are large pores in a pit membrane for a wide range of T_{PM} values?

Average values of R_{MIN} (R_{MIN_mean}) are very low in Scenario 1 of Model 1, with values < 4.5 nm for pit membranes of 150 to 1150 nm in thickness (Fig. 3a). The size of R_{MIN} declines considerably with increasing T_{PM}, and the largest values (R_{MIN_max}) decrease from radii of *c.* 20.4 ± 1.4 nm (standard deviation, σ_R) to 6 ± 0.6 nm (Fig. 3a). R_{MIN_max} values are at least 2.4 times and up to 4.9 times larger than the R_{MIN_mean} values, decreasing with T_{PM} (Fig. 3a). The likelihood of having an effective diameter ≥ 35 nm approaches zero (0.00005 ± 0.00009, Fig. 3b) when T_{PM} is > 220 nm, or the number of layers ≥ 6, and this therefore only occurs in 0.2 out of 12 000 pores.

For Scenario 2 of Model 1, a similar decline of R_{MIN} with increasing T_{PM} is found (Fig. S3), but with steeper declining likelihood values for large pores with T_{PM}. For a T_{PM} of 220 nm the likelihood of containing a large pore (defined in Scenario 2 of Model 1 as ≥ 180 nm in diameter) is nearly zero.

How does T_{PM} relate to measured embolism resistance?

The values of T_{PM_mean} vary from 165 nm (± 18 σ_R) for *Tilia platyphyllos* to 610 nm (± 79 σ_R) for *Olea europaea*, and the median of T_{PM} is equal to 270 nm ($n = 31$ species studied; Table S1). The value of T_{PM_centre} is always larger than the value of T_{PM_edge}, with an average difference of 105 nm, varying from

Table 2 Overview of the abbreviations used in modelling and experimental parameters used with reference to their units and definitions.

	Units	Definition
Modelling acronyms		
n		Sample size
N_L	–	Number of microfibril layers in a pit membrane; $N_L = (T_{PM} + 20)/40$
N_{PIT}	–	Average number of intervessel pits for a vessel with average length and diameter
P	–	Probability of encountering at least one hole larger than a given threshold in any given layer of a pit membrane.
P_{LP}	–	Probability of a leaky pit membrane occurring in an average vessel
R_{MIN}	nm	Radius of the narrowest constriction in a pore
R_{MIN_max}	nm	Maximum R_{MIN} value of all pores in a single pit membrane
R_{MIN_mean}	nm	Mean R_{MIN} value of all pores in a single pit membrane
t	–	Minimum size of a pore, a pore constriction, or a hole considered to be 'large'
μ_R, σ_R, R_L	nm	Parameters of the left-truncated normal distribution modelling pore constriction radii in Model 1
Experimental acronyms		
A_P	mm^2	Total intervessel pit membrane surface area for a vessel with average length and diameter
P_{12}, P_{50}, P_{88}	MPa	Xylem water potential corresponding to 12%, 50% and 88% loss of maximum hydraulic conductivity, respectively
T_{PM_mean}, T_{PM_centre}, T_{PM_edge}	nm	Intervessel pit membrane thickness as measured on transmission electron microscopy (TEM) images of freshly embedded xylem samples; mean value, value around the centre, and value near the edges for a pit membrane (excluding pit membrane annuli)
σ_R		Standard deviation

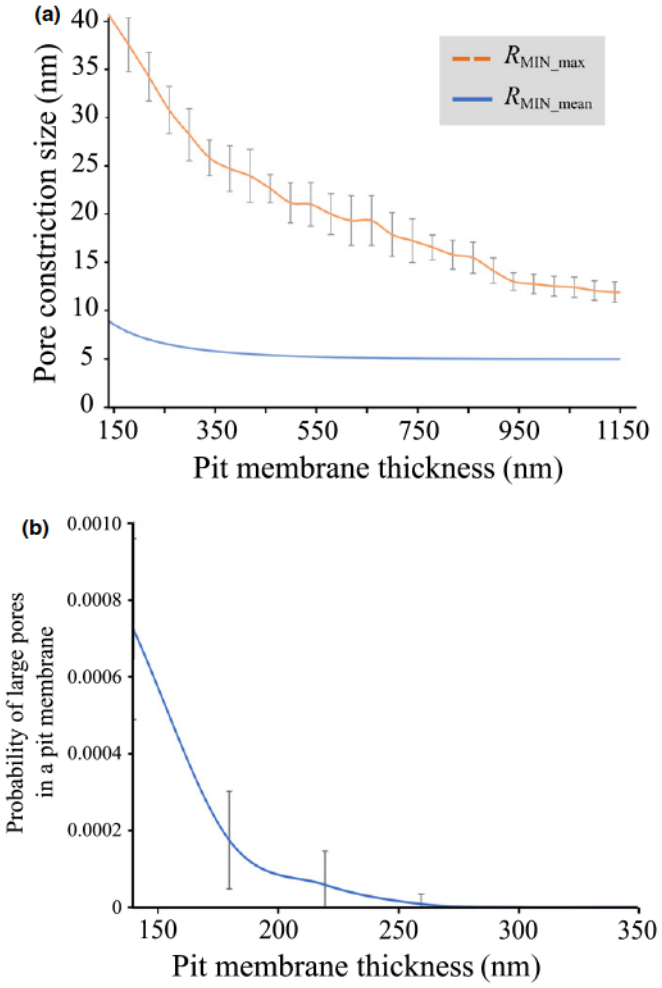

Fig. 3 Results of Scenario 1 of Model 1, showing the pit membrane thickness plotted against the pore constriction diameter based on Model 1 (a), and the likelihood of a relatively large R_{MIN_max} (≥ 17.5 nm) within a pit membrane (b), which decreased exponentially from 0.0008 ± 0.0002 (σ_R) to values approaching zero with increasing pit membrane thickness. A random number model was used, with mean pore constriction size set to 20 ± 15 nm, and a minimum size of 5 nm. Pore constriction sizes were determined 10 times for 12 000 simulated pores, corresponding to an average sized pit membrane.

2.1 nm (*T. platyphyllos*) to 297 nm (*O. europaea*), and this difference increases with T_{PM}. While there is no relationship between T_{PM_centre} and the coefficient of variation of T_{PM_centre} (Pearson's correlation coefficient, r (29) = 0.09, $P > 0.05$), the range between minimum and maximum values of T_{PM} measured within a tissue strongly increases with increasing T_{PM} (r (29) = −0.79, $P < 0.001$). Thus, the species with the thinnest and thickest pit membranes give a T_{PM} range of 80 nm (*T. platyphyllos*) to 497 nm (*O. europaea*).

When considering the whole dataset of the 31 species studied, P_{50} values are strongly related to the values of T_{PM_centre} (Table 3; Fig. 4a), with a logarithmic regression showing an R^2 value of 0.57 (F(2, 29) = 32.0, $P < 0.001$). An outlier in the T_{PM} vs P_{50} relationship includes *Corylus avellana*, which shows considerably high T_{PM} values of *c.* 400 nm for a P_{50} value of −2.02 MPa. Slightly lower correlations are found between the T_{PM_centre} and

Table 3 Overview of the *r*- and R^2-values between pit anatomical characteristics and embolism resistance.

	P_{12}	P_{50}	P_{88}	*Slope*	T_{PM_centre} range
T_{PM_centre}	0.46***,1	0.57***,1	0.54***,1	0.49***,2	0.79***,3
T_{PM_mean}	0.44***,1	0.56***,1	0.53***,1	0.48***,2	–
T_{PM_edge}	0.31**,1	0.41***,1	0.39***,1	0.34***,2	–
A_P	0.30*,1	0.25*,1	0.22*,1	0.10***,2	–
$P_E\_R_{MIN\_max}$	0.64***,3	0.73***,3	–	–	–
$P_E\_R_{MIN\_mean}$	0.67***,3	0.74***,3	–	–	–

Anatomical measurements include mean values of the intervessel pit membrane thickness (T_{PM_mean}), central pit membrane thickness (T_{PM_centre}), and pit membrane thickness near the annulus (T_{PM_edge}). Embolism resistance is quantified as the xylem water potential values corresponding to 12% (P_{12}), 50% (P_{50}), and 88% (P_{88}) loss of the maximum hydraulic conductivity based on vulnerability curves. The estimation of embolism propagation pressure (P_E) is either based on the largest value of R_{MIN} across all pores of a membrane ($P_E\_R_{MIN\_max}$) or the mean value of R_{MIN} across all pores of a membrane ($P_E\_R_{MIN\_mean}$), using a modified Young–Laplace equation. A_P, total intervessel pit membrane surface area for a vessel with average length and diameter. Only the regressions and correlations that show the strongest relationships are given here. Asterisks indicate significant difference (*, $P < 0.05$; **, $P < 0.01$; ***, $P < 0.001$; –, irrelevant and not analysed). For more detailed definitions of the acronyms used in this table, see Table 2.
[1]Logarithmic regression.
[2]Power regression.
[3]Pearson correlation coefficient.

P_{12} (F(2, 29) = 24.4, R^2 = 0.46, $P < 0.001$), and between T_{PM_centre} and P_{88} (F(2, 29) = 34.2, R^2 = 0.54, $P < 0.001$; Table 3; Fig. 4a). The T_{PM_centre} values show a stronger relationship to embolism resistance than T_{PM_mean} and T_{PM_edge}. The average intervessel pit membrane surface area per vessel (A_P, Table S1) shows much weaker correlations with P_{12}, P_{50}, and P_{88} than any T_{PM} trait, with the strongest correlation between A_P and P_{12} (F(2, 18) = 7.75, R^2 = 0.30, $P < 0.05$; Table 3).

When limiting our dataset to species with an average intervessel pit membrane surface area per vessel (A_P) value, no linear correlation between P_{12}, P_{50}, or P_{88} and A_P can be found (Fig. 4c), whereas the negative correlations between pit membrane thickness (T_{PM_mean}, T_{PM_centre}, and T_{PM_edge}) and P_{12}, P_{50}, and P_{88} are highly significant (Table 4, Fig. 4b).

Furthermore, we find a power regression with an R^2–value of 0.48 between the slope of vulnerability curves and T_{PM_mean} (F(2, 29) = 88.4, R^2 = 0.48, $P < 0.001$; Table 3), with a decreasing slope being associated with increasing T_{PM_mean}. T_{PM_centre} and T_{PM_mean} have a stronger relationship with the slope than T_{PM_edge} (Table 3). Thus, thicker pit membranes result in more negative P_{50} values and a smaller slope, with T_{PM} mainly affecting P_{50}, and less P_{12} and P_{88}.

Do modelled and measured embolism resistance correspond to each other for a wide range of T_{PM}?

There are clear differences in the estimated pressures that would induce embolism spreading, depending on the surface tension and whether the maximum or mean R_{MIN} values are considered

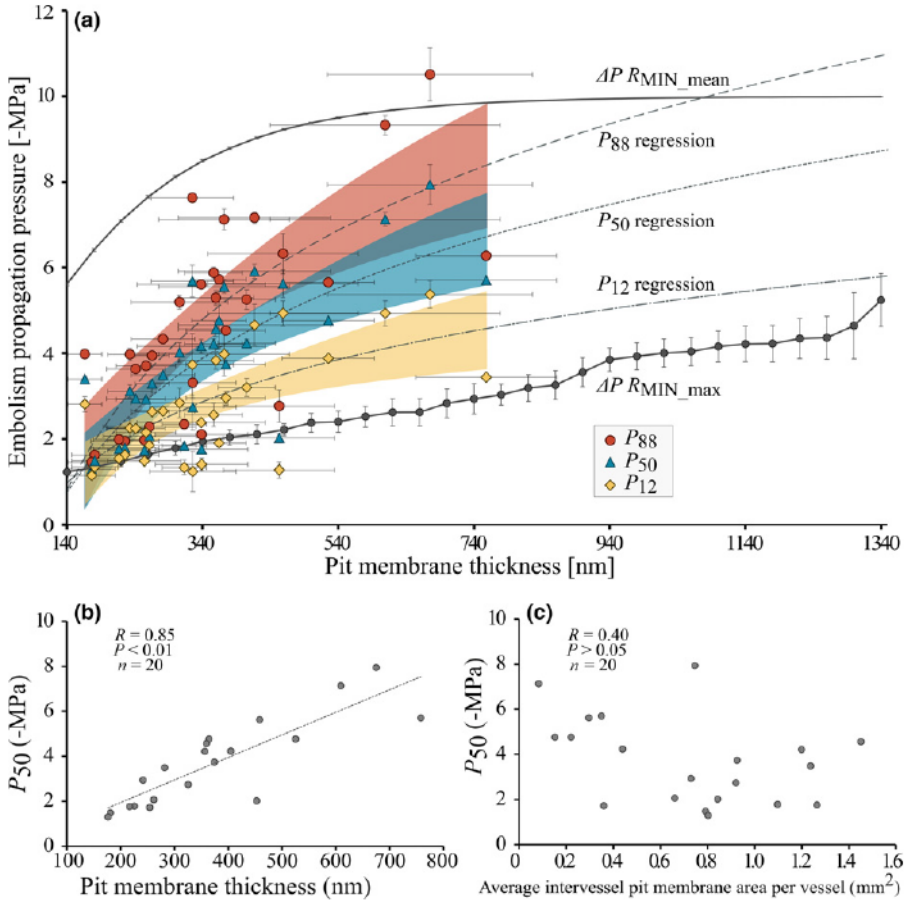

Fig. 4 The relationship between central pit membrane thickness (T_{PM_centre}) and modelled and measured embolism resistance based on 31 angiosperm species (a), the relationship between P_{50} values and T_{PM_centre} (b), and P_{50} vs the intervessel pit membrane area per vessel (A_P, c). The data plotted in (b) and (c) are based on the same 20 species and can be directly compared. Modelled embolism propagation pressures rely on the largest values of R_{MIN_max}, and R_{MIN_min} with σ_R values (solid lines) based on all pores in a single pit membrane with variable thicknesses according to Model 1. A modified Young–Laplace equation is used to estimate the embolism propagation pressure for a surface tension of 25 mN m^{-1} (a). P_{12}, P_{50} and P_{88} values with SE values (intraspecific variability) are based on a flow-centrifuge method or microCT images and are plotted against T_{PM_centre} measurements with σ_R values (intra-tissue variability). T_{PM_centre} was based on data obtained from transmission electron microscopy (TEM). Logarithmic regression lines are shown as dashed grey lines, with corresponding confidence intervals (P_{12}, yellow; P_{50}, blue; P_{88}, red) in (a). The values in (b) and (c) are given for a linear correlation.

(Fig. 4a). For a surface tension of 72 mN m^{-1}, estimated pressures of embolism spreading, which may largely correspond to P_{12}, are much higher than the measured P_{12} values, and are even higher than the measured P_{50} values (Fig. S4). Regression lines of the T_{PM}–P_{12}, T_{PM}–P_{50} and T_{PM}–P_{88} relationships, however, fall well within the estimated embolism propagation pressures when a surface tension of 25 mN m^{-1} (Fig. 4a) is considered. Although absolute values of modelled and measured embolism resistance (P_{12} and P_{50}) do not match (Figs 4a, 5), they are significantly related to each other (P_{12} to R_{MIN_mean} and R_{MIN_max}: r (29) = 0.67 and r (29) = 0.64, $P < 0.01$; P_{50} to R_{MIN_mean} and R_{MIN_max}: r (29) = 0.74 and r (29) = 0.73, $P < 0.001$; Table 3; Fig. 5). When R_{MIN_max} is considered, estimated pressures related to embolism spreading show a small range, with values of *c.* 1.2 MPa for a T_{PM} of 140 nm and up to 2.7 MPa for a T_{PM} of 758 nm (Fig. 5b), which underestimates embolism resistance (Figs 4a, 5a,b). Much higher embolism propagation pressures, between 5.6 and 10 MPa, are obtained for estimations based on R_{MIN_mean}, thus overestimating embolism resistance (Fig. 5c,d). There is a clear upper limit to embolism propagation pressure for R_{MIN_mean} at *c.* 10 MPa, which is achieved for pit membranes with thicknesses ≥ 600 nm (Fig. 4a).

Modelled embolism propagation pressures based on R_{MIN_max} are similar but are typically lower than the experimental values (Fig. 5a,b). Estimated embolism propagation pressures based on R_{MIN_max} are especially close to measured embolism resistance for number of species whose P_{12} and P_{50} values are less negative (Fig. 5a,b), while estimated embolism propagation pressures based on R_{MIN_mean} are much higher than P_{12} and P_{50} measurements (Fig. 5c,d).

How likely are leaky intervessel pit membranes at the vessel level?

Based on Model 2, the probability of having a leaky pit membrane in a vessel decreases exponentially with increasing T_{PM} (Figs 6, S5). For a fixed T_{PM}, the slope of the relationship between N_{PIT} and the probability of a leaky pore strongly

Table 4 Pearson correlation matrix presenting the *r*-values of linear correlations between embolism resistance ($-P_{12}$, $-P_{50}$, $-P_{88}$), average intervessel pit membrane surface area per vessel (A_P), and pit membrane thickness measurements (T_{PM_mean}, T_{PM_centre}, T_{PM_edge}).

	A_P	T_{PM_mean}	T_{PM_centre}	T_{PM_edge}	$-P_{12}$	$-P_{50}$	$-P_{88}$
A_P	1						
T_{PM_mean}	−0.44	1					
T_{PM_centre}	−0.48*	(1.00**)	1				
T_{PM_edge}	−0.32	(0.96**)	0.94**	1			
$-P_{12}$	−0.33	0.72**	0.75**	0.58**	1		
$-P_{50}$	−0.40	0.83**	0.85**	0.70**	0.92**	1	
$-P_{88}$	−0.36	0.81**	0.83**	0.70**	0.90**	0.99**	1

Only 20 species for which we obtained A_P values were considered. The extended dataset (n = 31 species) is provided in Supporting Information Table S1. Since T_{PM_mean} is calculated based on the thickness at the centre and the edge, correlations between T_{PM_mean} with T_{PM_centre} and T_{PM_edge} should not be considered and are given in brackets. A_P, total intervessel pit membrane surface area for a vessel with average length and diameter; P_{12}, P_{50} and P_{88}, xylem water potential values corresponding to a 12%, 50%, 88% loss of maximum hydraulic conductivity, respectively. T_{PM}, pit membrane thickness; T_{PM_mean}, mean pit membrane thickness; T_{PM_centre} membrane thickness at the centre of the pit; T_{PM_edge}, membrane thickness at the edge. For more detailed definitions, see Table 2. Asterisks indicate significant difference (*, $P < 0.05$, **, $P < 0.01$).

depends on T_{PM} (Fig. S6): steep, exponential slopes are found for thin pit membranes, while low, more linear slopes are found for thick pit membranes. Therefore, T_{PM_mean} and N_{PIT} affect the likelihood of large effective pore radii differently, with N_{PIT} having an unequal effect on the likelihood of having leaky pit membranes.

For the 0.5 likelihood assumption (Figs S5, S6b), vessels with 820 nm thick pit membranes reach a likelihood of having a leaky pit membrane below 0.20, even in vessels with 400 000 intervessel pits, which means that not even every fifth vessel would have a leaky pit.

For the 0.25 likelihood of Model 2 (Figs 6, S6a), an exponential change is found for T_{PM_mean} values between 200 and 300 nm, while little or no effect is seen for T_{PM_mean} values < 200 nm or > 350 nm. The high and low probability plateaus in the three-dimensional graphs of Model 2 (Figs 6, S5) suggest the existence of a thin and a thick T_{PM} range that typically results in leaky or very safe, nonleaky vessels, respectively, independent of N_{PIT}. At the exponential phase of the three-dimensional graph in Fig. 6, an increase in N_{PIT} from 3000 to 70 000 (i.e. a 23-fold increase) is equivalent to adding approx. five additional microfibril layers to a pit membrane (i.e. an increase in T_{PM} of 180 nm). Critical T_{PM} values are higher for the 0.5 likelihood of Model 2 (Figs S6b, S5), with the largest effect of N_{PIT} for pit membranes between 500 and 700 nm.

The results obtained from Model 3 show that the modelled probability of encountering leaky pit membranes in a vessel with 30 000 intervessel pits (N_{PIT}) decreases exponentially for T_{PM} values > 180 nm or > 260 nm when assuming 5 or 10 holes per microfibril layer, respectively (Fig. 7). Assuming 5 or 10 holes per layer, < 1 out of 30 000 pits has a large pore for T_{PM} values > 220 nm and > 340 nm, respectively. Therefore, 220 nm thick pit membranes with 5 holes per layer are approximately as safe as 340 nm thick pit membranes with 10 holes per layer. When directly comparing Models 2 and 3 using 30 000 as the value for N_{PIT}, a more-or-less similar probability of encountering a large pore in a vessel is found for the 0.25 likelihood scenario of Model 2 and the 10 holes per layer in Model 3 (Fig. 7).

Discussion

The results described here indicate that the chance of having large pores in pit membranes decreases strongly with the number of constrictions, and therefore with T_{PM} (Hypothesis 1). This finding is independent of the actual size of pore constrictions and is supported by a strong relationship between embolism resistance and T_{PM} (Jansen *et al.*, 2009, 2018; Lens *et al.*, 2011; Scholz *et al.*, 2013; Li *et al.*, 2016a,b; Schuldt *et al.*, 2016). Modelled embolism propagation values are significantly correlated with measured embolism resistance values (Hypothesis 2), although they differ in terms of absolute values. There is a good agreement when the dynamic surface tension of xylem sap is taken into account (Yang *et al.*, 2020), but embolism spreading does not seem to represent a function of pore constriction size (R_{MIN_max} and R_{MIN_mean}) only. Our results also suggest that the likelihood of having a leaky pit membrane within a vessel is extremely low (Hypothesis 3) and is mainly determined by T_{PM}. Overall, pore constrictions provide a mechanistic explanation of why embolism resistance is correlated with T_{PM}, and why pit membranes provide hydraulic safety to angiosperm xylem.

The most narrow pore constriction becomes strongly reduced in size with increasing pit membrane thickness

The three models developed here show a negative correlation between the simulated pore sizes and T_{PM}, which is reflected in a low probability of large pores, both at the level of an individual pit membrane and an entire vessel. Based on Model 1, the chance of having a large pore in a pit membrane thicker than 180 nm is close to zero. Interestingly, the thinnest pit membranes measured in this study (*c.* 165–180 nm) are likely to represent a lower limit for T_{PM}, since earlier records of T_{PM} values below 150 nm (Jansen *et al.*, 2009; Li *et al.*, 2016a,b) are likely artefacts resulting from shrinkage (Zhang *et al.*, 2017, 2020; Kotowska *et al.*, 2020). Thus, angiosperm pit membranes seem to have at least four or five layers of cellulose microfibrils and pore constrictions, which keeps the number of large pores very low for most species. There is a clear conceptual relationship between the thickness of

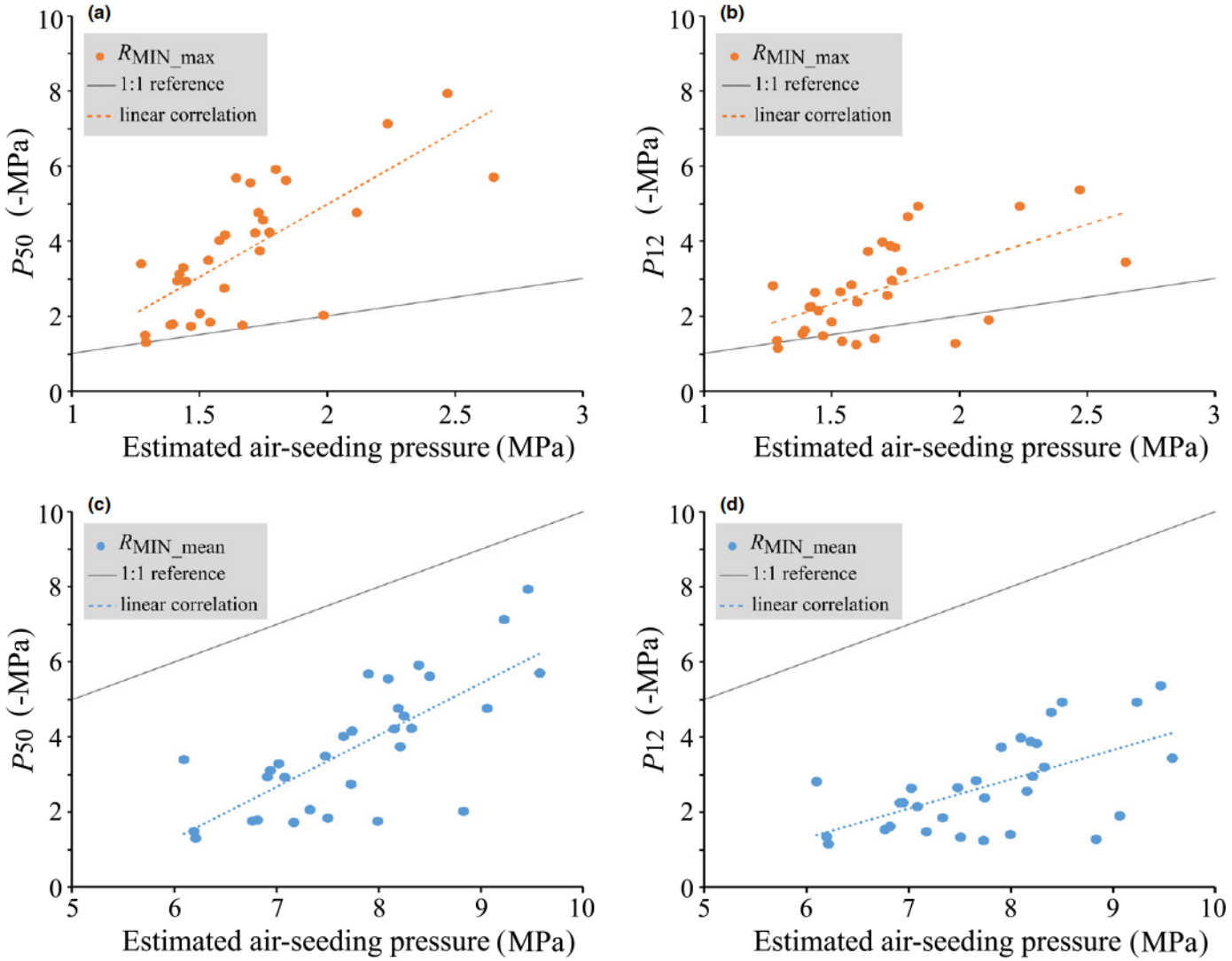

Fig. 5 Modelled embolism propagation pressure based on R_{MIN_max} (a, b; orange) and R_{MIN_mean} (c, d; blue) following Scenario 1 of Model 1 vs measured values of P_{50} (a, c) and P_{12} (b, d) for 31 angiosperm species. The 1 : 1 reference line is shown as a black dotted line, and the linear regression lines are dashed blue/orange lines.

a fibrous porous medium and the size of the narrowest pore constriction, as also seen for nonwoven, fibrous geotextiles that differ in thickness (Aydilek *et al.*, 2007).

Model 2 suggests that the probability of encountering large pores in intervessel pit membranes of an average vessel follows an exponential pattern over a fairly narrow range of T_{PM}, with critical T_{PM} values between 200 to 300 nm and 500 to 700 nm for a 0.25 and 0.50 likelihood, respectively, of having at least one hole larger than t within a single microfibril layer. Although this likelihood cannot be accurately determined due to our limited understanding of embolism spreading and the ultrastructure of pit membranes, we believe that a realistic likelihood would probably lay around 0.25, with 0.50 being too conservative. This assumption is supported by the steeper increase in embolism resistance within the lower T_{PM} range between 140 and 340 nm than in the higher T_{PM} range, and by the probabilities of large pores in pit membranes approaching zero for $T_{PM} > 250$ nm in Models 1 and 3. We applied a logarithmic regression between P_{12}, P_{50}, P_{88} and T_{PM} (Fig. 4a), unlike a linear scaling that was previously suggested (Lens *et al.*, 2011; Li *et al.*, 2016a,b). Interestingly, this logarithmic regression has P_{50} values approaching 10 MPa for a T_{PM} of > 1350 nm, which corresponds to the upper physical limit of both xylem water potential and the maximum measured T_{PM} value for angiosperms (Vilagrosa *et al.*, 2003; Jansen *et al.*, 2009; Kanduč *et al.*, 2020).

A clear limitation of Models 1 and 2 is that the alignment of pore constrictions or holes across all layers of a pit membrane is not considered. Although we do not know whether alignment across different layers is required for mass flow of air across a pit membrane, misalignment could enormously reduce the probability of having a leaky pit membrane and increase tortuosity, because the assumed 20 nm distance between the layers in all three models is low compared to the hole size in Models 2 and 3. Thus, applying stricter criteria to Model 3, such as larger overlap of holes across all layers to obtain a geodesic tortuosity that would be close to 1 (Zhang *et al.*, 2020), would lead to considerably

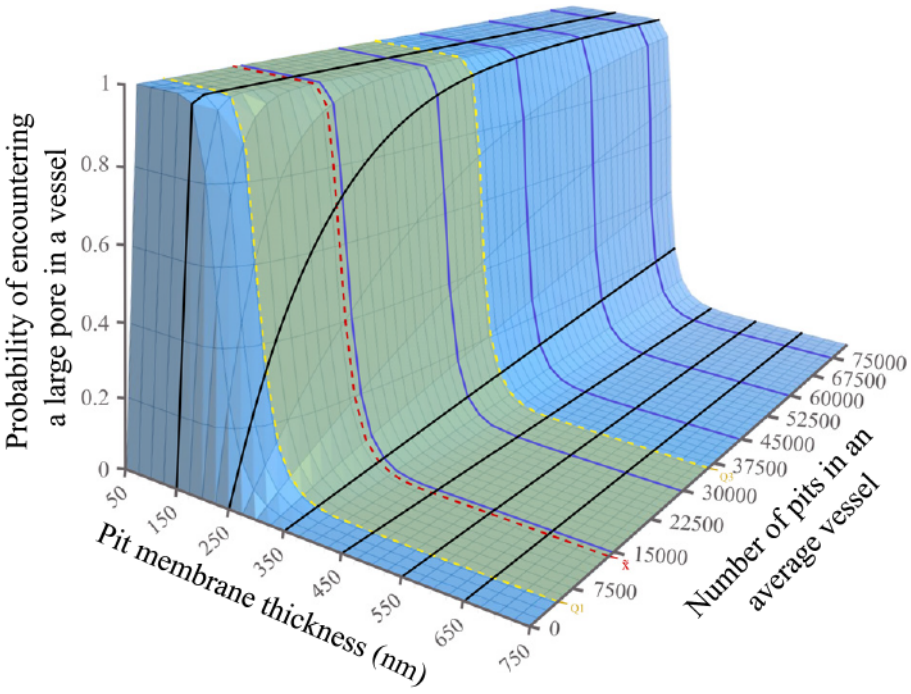

Fig. 6 The probability of encountering at least one pore with a large effective diameter in intervessel pit membranes for an entire vessel decreases with increasing pit membrane thickness (black lines), but increases with an increasing number of pits (blue lines), according to Model 2. The likelihood of having a large hole within a single microfibril layer was assumed to be ≤ 0.25. This model assumed that the number of cellulose layers in pit membranes increases with pit membrane thickness, did not consider the actual size of the pore constriction, and ignored whether or not a hole was aligned with other holes in adjacent pit membrane layers. The green area indicates where most angiosperm species lie, based on the number of intervessel pits per vessel, with the median indicated by the red dotted line, and the first and third quartiles indicated by yellow dotted lines.

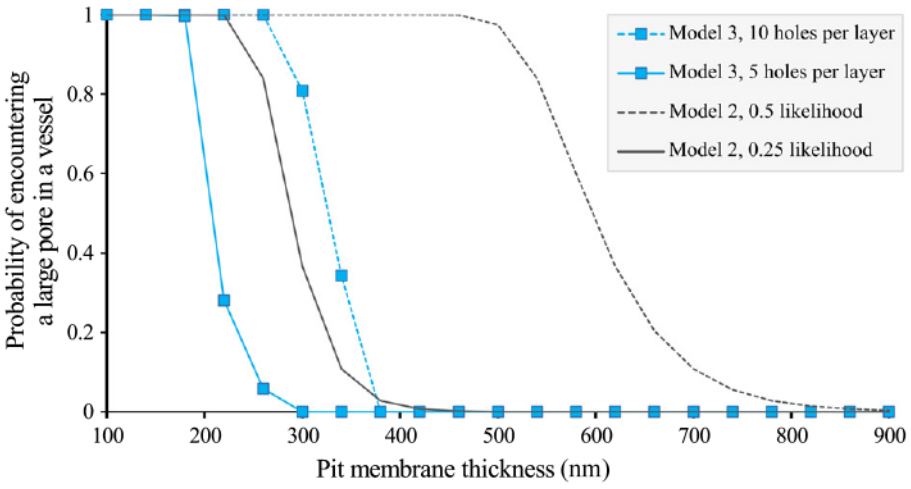

Fig. 7 Comparison of the results from Models 2 and 3, showing for a wide range of pit membrane thicknesses the probability of encountering a large pore in a vessel with 30 000 intervessel pits. For each model, 2 scenarios are given: a 0.25 and 0.5 likelihood of having a large hole in a pit membrane layer, without alignment of holes and no exact hole size (Model 2), and the occurrence of either 5 or 10 holes of 100 nm in diameter in a single pit membrane layer, with hole alignment as a requirement (Model 3).

lower probabilities of leaky pit membranes in a vessel. Nevertheless, even the low amount of overlap applied demonstrates that the chance of having a leaky vessel with 30 000 intervessel pit membranes drastically decreases when T_{PM} values are *c.* 250 nm (Fig. 7; 0.25 likelihood scenario of Model 2, Model 3). Since the 0.5 likelihood scenario of Model 2 shows a decrease in leakiness at much higher T_{PM} values than the other models, we consider the predictive value and applicability of this scenario as rather low. It is possible that variation in T_{PM} within a vessel or within the vessel network provides additional chances of leakiness, and small differences in T_{PM} across organs (Kotowska *et al.*, 2020) could influence embolism resistance. Capturing this variation, however, is difficult because measuring T_{PM} may not be straightforward, for instance due to TEM preparation artefacts, aggregation of cellulose fibrils into larger aggregates, and seasonal shrinkage of pit membranes (Schmid & Machado, 1968; Sorek *et al.*, 2021).

The difference between central and marginal T_{PM} questions the modelling assumption of equally spaced cellulose fibres. The slightly negatively charged cellulose fibres may repel each other and are more loosely arranged in the centre than near the edges (Zhang *et al.*, 2016), where the fibres are firmly anchored into the pectin-rich annulus and primary wall. Although the orientation of microfibrils may not be completely random and appears to be directed by a dual guidance mechanism (Chan & Coen, 2020), it seems unlikely that more cellulose fibrils are deposited in the centre than near the annulus, in contrast to torus-bearing angiosperms (Dute, 2015).

How is the size of pore constrictions linked to embolism resistance?

Embolism propagation across pit membranes is strongly dependent on T_{PM} and the number of pit membrane layers, which

control the size of the narrowest pore constriction within a pore. Pit membranes are not different from other nonwoven, fibrous porous media, where the pressure required to force a gas bubble through the medium, the so-called bubble point, is a function of the thickness of the medium and its overall structure (Aydilek *et al.*, 2007). Comparisons of modelled embolism propagation pressures with measurements of P_{12}, P_{50} and P_{88} show strong correlations but clear differences in absolute values for most species (Fig. 5), with P_{12}, P_{50} and P_{88} values falling between the modelled embolism propagation based on R_{MIN_mean} and R_{MIN_max} (Figs 4a, 5b,d). As could be expected, P_{12} values were closest to estimated values based on R_{MIN_max}. In general, this correlation illustrates that our assumptions in Model 1 are fairly well related to real embolism propagation pressures in plants. Despite the simplicity of the three-dimensional models in this study and the modified Young–Laplace equation, it is remarkable that our modelled R_{MIN} values of embolism resistance largely agree with experimental values, without accounting for variables such as dynamic surface tension of xylem lipids, bubble snap-off, changes in temperature, gas solubility, and other xylem anatomical traits. Experimental data on the pressure that is needed to induce embolism in angiosperm xylem shows values between 0.4 and 2 MPa (Choat *et al.*, 2004; Jansen *et al.*, 2009; Christman *et al.*, 2012; Wason *et al.*, 2018), which is more or less in line with P_{12} values for a wide range of angiosperm species (Bartlett *et al.*, 2016). Moreover, 65% of the species in our study show P_{12} values that are more negative than −2 MPa, with an average P_{12} value of −2.57 MPa, which matches the average P_{12} value of −2.65 MPa of 12 temperate angiosperm species (Schuldt *et al.*, 2020).

Embolism propagation across thin pit membranes seems to be determined by pores similar in size to R_{MIN_max} due to the high similarity between measurements of P_{12} and P_{50} with modelled embolism resistance based on R_{MIN_max}. By contrast, embolism spreading in species with thick pit membranes is affected by pore sizes that can be close to both R_{MIN_max} and R_{MIN_mean} (Figs 3b, 4a). This finding is in line with the fact that high values of T_{PM_mean} show a higher standard deviation than low T_{PM_mean} values, while the slope of vulnerability curves becomes lower for species with thicker pit membranes. In addition, the standard error values of P_{12}, P_{50}, and P_{88} tend to increase with increasing embolism resistance (Table S1), that is, higher variation in embolism resistance and lower slopes for embolism resistant species could be linked to increasing variation in T_{PM} for species with thick pit membranes. In fact, R_{MIN_mean} is expected to provide an upper limit for embolism resistance, since it is unlikely that pore constrictions smaller than average values (i.e. < R_{MIN_mean}) will determine embolism spreading. Accordingly, R_{MIN_max} offers the least resistance to mass flow of gas moving through a pore space, and provides a good explanation for a lower limit to embolism spreading.

There are three possible reasons why modelled embolism resistance does not match the absolute values of the measured P_{12} values, and these reasons may not be mutually exclusive. First, the values obtained from Model 1 are based on embolism propagation estimates for a single pit membrane model with a certain thickness, while P_{12} and P_{50} values represent hydraulically weighted losses of conductivity at the vessel network level, which is affected by various structural xylem parameters, such as vessel grouping and the ratio of T_{PM} to pit membrane area (Levionnois *et al.*, 2021).

Second, estimations based on the Young–Laplace equation should be interpreted with caution due to various poorly known parameters and processes when applying this formula to xylem conduits. Embolism formation in a multiphase environment under negative pressure is highly complicated by, for instance, dynamic surface tension, line tension, the contact angle of the gas–liquid interface within the pit membrane, and highly variable pore sizes (Choat *et al.*, 2004; Law *et al.*, 2017; Schenk *et al.*, 2017; Satarifard *et al.*, 2018; Li *et al.*, 2020; Yang *et al.*, 2020; Zhang *et al.*, 2020). Moreover, pore constrictions and porosity could change if pit membranes become deflected and aspirated against the pit border, which could cause pit membrane shrinkage, reduced porosity and constrictivity, or rearrangement of microfibrils (Tixier *et al.*, 2014; Zhang *et al.*, 2017, 2020; Kotowska *et al.*, 2020). However, the mechanical properties of pit membranes remain largely unknown (Tixier *et al.*, 2014).

Third, it is also possible that drought-induced embolism spreading does not occur via mass flow of air–water menisci across intervessel pit membranes, as suggested by the air-seeding hypothesis. The discovery of surfactant-coated nanobubbles in xylem sap provides a complementary mechanism of the mass flow of gas, and highlights the importance of amphiphilic, insoluble lipids associated with pit membranes, and bubble snap-off by pore constrictions (Schenk *et al.*, 2015, 2017, Schenk *et al.* 2018, Schenk *et al.*, 2021; Kaack *et al.*, 2019; Park *et al.*, 2019). Moreover, diffusion of gas molecules between an embolised and an adjacent vessel could represent an additional way in which gas entry could trigger embolism formation (Guan *et al.*, 2021), which might be largely dependent on R_{MIN_mean} and less so on R_{MIN_max}.

Pit membrane thickness and the number of intervessel pits have different consequences on embolism resistance

We show that T_{PM} is a much stronger determinant of the likelihood of leaky pit membranes than the number of pits per vessel (N_{PIT}) and the total intervessel pit membrane surface area (A_P; Table 4; Fig. 4c). Therefore, our results do not support the rare pit hypothesis (Wheeler *et al.*, 2005; Sperry *et al.*, 2006) but provide a novel view of the relationships between N_{PIT} and embolism resistance, and A_P and embolism resistance. Most importantly, our Model 2 shows that T_{PM} and N_{PIT} affect the likelihood of encountering wide pores differently, with contrasting differences for species with a wide range of T_{PM} values. The effect of N_{PIT} on vessel leakiness is limited to a narrow range of critical T_{PM} values, depending on the assumptions made in Model 2 (Figs 6, S5). The idea that large A_P values lead to a high probability of large pore constrictions in a vessel can be applied to a certain range of T_{PM} values. However, the hypothesis that large A_P values increase the probability of large pores in each single vessel is highly doubtful based on the available evidence.

In a general, simplified way, three functional types of intervessel pit membranes can be distinguished based on T_{PM} (Model 2): (1) a thin, risky type, with relatively large pore constrictions, rather low embolism resistance, and little or no reduced embolism resistance for a low number of intervessel pits, (2) a thick and very safe pit membrane type, with narrow pore constrictions, high embolism resistance, and hardly any reduction of embolism resistance for a high number of intervessel pits, and (3) an intermediate pit membrane type, with embolism resistance strongly affected by N_{PIT}, where N_{PIT} or other xylem structural traits could potentially be modified during growth to vary embolism resistance in response to the amount of drought experienced. Unfortunately, the exact T_{PM} values that would define these pit membrane types are unclear. Based on leakiness probabilities that are close to zero for $T_{PM} > 250$ nm based on Model 1 and Scenario 1 of Model 3 (Figs 3 and 7), and due to the decreasing slopes of the measured P_{50} values with increasing T_{PM}, we roughly estimate that T_{PM} values of the intermediate type are between 150 and 300 nm, which is where the high probability drops from 1 to almost 0 in Fig. 6. This would correspond to 60% of the species in our data set.

Interestingly, embolism resistance in the risky and safe pit membranes (types 1 and 2) is either not affected or is weakly affected by the number of intervessel pits. Since the number of intervessel pits is associated with hydraulic connectivity, which in turn affects hydraulic conductivity and thus efficiency (Loepfe *et al.*, 2007; Mrad *et al.*, 2018), this finding suggests that hydraulic safety can be uncoupled from hydraulic efficiency. In other words, for a given T_{PM}, and with considerable variation in N_{PIT}, hydraulic conductivity could be affected much more by N_{PIT} than by hydraulic safety (Fig. 6, Fig. S6). Hence, Model 2 provides a novel view on the weak relationship between specific hydraulic conductivity and P_{50} values for many angiosperm species (Hacke *et al.*, 2006; Loepfe *et al.*, 2007; Gleason *et al.*, 2016; Sanchez-Martinez *et al.*, 2020). It would also be interesting to examine whether considerable variation in T_{PM} and N_{PIT} leads to considerable variation in the hydraulic resistance of pit membranes.

The rare pit hypothesis relies on the assumption that for successful embolism propagation, there is always at least one large pore per successive intervessel wall within the xylem network. Our results indicate that the rare pit hypothesis cannot explain embolism propagation at the level of the whole vessel network, since the functional importance of multiple pore constrictions makes it highly unlikely that many vessels contain a large pore for a wide range of T_{PM}. In fact, earlier studies that tested the rare pit hypothesis should be considered carefully due to possible artefacts in embolism resistance measurements (Wheeler *et al.*, 2013; Torres-Ruiz *et al.*, 2017). Also, no large pores have ever been found in hydrated pit membranes (Schmid & Machado, 1968; Choat *et al.*, 2003, 2004; Pesacreta *et al.*, 2005; Jansen *et al.*, 2018; Zhang *et al.*, 2020). Finally, primary cell wall development, including the assembly and deposition of cellulose fibrillar aggregates, require highly redundant processes involving the cytoplasm and its cytoskeleton, reducing the likelihood of large gaps in primary cell walls (Chaffey *et al.*, 1997; Oda & Fukuda, 2013; Bourdon *et al.*, 2017; Sugiyama *et al.*, 2017, 2019).

Further progress in understanding embolism spreading in angiosperm xylem will strongly depend on the development of realistic three-dimensional pit membrane and vessel network models (Gaiselmann *et al.*, 2014; Mrad *et al.*, 2018; Li *et al.*, 2020), combined with careful simulations of the chemical and physical interactions within a multiphase environment of gas, water, cellulose, and surfactants.

Acknowledgements

Financial support is acknowledged to SJ by a research grant from the Deutsche Forschungsgemeinschaft (DFG, German Research Foundation, project number 383393940), to SJ and VS by the Baden-Württemberg Ministerium für Wissenschaft, Forschung und Kunst (project number 7533-7-11.10-16), and to HJS and SJ by the National Science Foundation (IOS-1754850). We thank Klaus Körber from the Bavarian State Institute for Viticulture and Horticulture, Veitshochheim, Germany, for granting us access to the Stutel-Arboretum facility, as well as Andreas Lösch and all others involved in the 'Klimabäume Stutel' project. We thank various colleagues and three reviewers for fruitful discussions and valuable suggestions. We also thank Jarmila Pittermann, the handling editor, for overseeing the editorial process at *New Phytologist*.

Author contributions

LK, MW, LP, HJS, VS and SJ planned and designed the research. EI, ZK, SL, CLT, YZ and BS provided experimental data. LK and MW wrote the manuscript, with input from all co-authors. LK and MW contributed equally to this work.

ORCID

Emilie Isasa https://orcid.org/0000-0002-5927-5151
Steven Jansen https://orcid.org/0000-0002-4476-5334
Lucian Kaack https://orcid.org/0000-0003-4705-2521
Zohreh Karimi https://orcid.org/0000-0003-3633-4099
Shan Li https://orcid.org/0000-0002-9853-163X
Luciano Pereira https://orcid.org/0000-0003-2225-2957
H. Jochen Schenk https://orcid.org/0000-0001-6261-2780
Bernhard Schuldt https://orcid.org/0000-0003-4738-5289
Christophe L. Trabi https://orcid.org/0000-0002-2538-3613
Matthias Weber https://orcid.org/0000-0001-6608-0857
Ya Zhang https://orcid.org/0000-0002-1617-4860

References

Aydilek AH, D'Hondt D, Holtz RD. 2007. Comparative evaluation of geotextile pore sizes using bubble point test and image analysis. *Geotechnical Testing Journal* **30**: 173–181.

Bartlett MK, Klein T, Jansen S, Choat B, Sack L. 2016. The correlations and sequence of plant stomatal, hydraulic, and wilting responses to drought. *Proceedings of the National Academy of Sciences, USA* **113**: 13098–13103.

Bourdon M, Kalmbach L, Helariutta Y. 2017. Plant vasculature: selective membrane-to-microtubule tethering patterns the xylem cell wall. *Current Biology: CB* **27**: R842–R844.

Brodersen CR, McElrone AJ, Choat B, Lee EF, Shackel KA, Matthews MA. 2013. *In vivo* visualizations of drought-induced embolism spread in *Vitis vinifera*. *Plant Physiology* **161**: 1820–1829.

Brodribb TJ, Bienaimé D, Marmottant P. 2016. Revealing catastrophic failure of leaf networks under stress. *Proceedings of the National Academy of Sciences, USA* **113**: 4865–4869.

Chaffey NJ, Barnett JR, Barlow PW. 1997. Cortical microtubule involvement in bordered pit formation in secondary xylem vessel elements of *Aesculus hippocastanum* L. (Hippocastanaceae): a correlative study using electron microscopy and indirect immunofluorescence microscopy. *Protoplasma* **197**: 64–75.

Chan J, Coen E. 2020. Interaction between autonomous and microtubule guidance systems controls cellulose synthase trajectories. *Current Biology* **30**: 941–947.e2.

Choat B, Badel E, Burlett R, Delzon S, Cochard H, Jansen S. 2016. Noninvasive measurement of vulnerability to drought-induced embolism by x-ray microtomography. *Plant Physiology* **170**: 273–282.

Choat B, Ball M, Luly J, Holtum J. 2003. Pit membrane porosity and water stress-induced cavitation in four co-existing dry rainforest tree species. *Plant Physiology* **131**: 41–48.

Choat B, Cobb AR, Jansen S. 2008. Structure and function of bordered pits: new discoveries and impacts on whole-plant hydraulic function. *New Phytologist* **177**: 608–626.

Choat B, Jansen S, Brodribb TJ, Cochard H, Delzon S, Bhaskar R, Bucci SJ, Feild TS, Gleason SM, Hacke UG *et al.* 2012. Global convergence in the vulnerability of forests to drought. *Nature* **491**: 752–755.

Choat B, Jansen S, Zwieniecki MA, Smets E, Holbrook NM. 2004. Changes in pit membrane porosity due to deflection and stretching: the role of vestured pits. *Journal of Experimental Botany* **55**: 1569–1575.

Christman MA, Sperry JS, Adler FR. 2009. Testing the 'rare pit' hypothesis for xylem cavitation resistance in three species of *Acer*. *New Phytologist* **182**: 664–674.

Christman MA, Sperry JS, Smith DD. 2012. Rare pits, large vessels and extreme vulnerability to cavitation in a ring-porous tree species. *New Phytologist* **193**: 713–720.

Dória LC, Meijs C, Podadera DS, Del Arco M, Smets E, Delzon S, Lens F. 2019. Embolism resistance in stems of herbaceous Brassicaceae and Asteraceae is linked to differences in woodiness and precipitation. *Annals of Botany* **124**: 1–14.

Dute RR. 2015. Development, structure, and function of torus–margo pits in conifers, ginkgo and dicots. In: Hacke U, ed. *Functional and ecological xylem anatomy*. Cham, Switzerland: Springer International Publishing, 77–102.

Esau K. 1977. *Anatomy of seed plants, 2nd edn.* New York, NY, USA: John Wiley & Sons.

Gaiselmann G, Tötzke C, Manke I, Lehnert W, Schmidt V. 2014. 3D microstructure modeling of compressed fiber-based materials. *Journal of Power Sources* **257**: 52–64.

Gleason SM, Westoby M, Jansen S, Choat B, Hacke UG, Pratt RB, Bhaskar R, Brodribb TJ, Bucci SJ, Cao K-F *et al.* 2016. Weak tradeoff between xylem safety and xylem-specific hydraulic efficiency across the world's woody plant species. *New Phytologist* **209**: 123–136.

Guan X, Pereira L, McAdam S, Cao KF, Jansen S. 2021. No gas source, no problem: pre-existing embolism may affect non-pressure driven embolism spreading in angiosperm xylem by gas diffusion. *Plant, Cell & Environment*. doi: 10.1111/pce.14016

Hacke UG, Sperry JS, Wheeler JK, Castro L. 2006. Scaling of angiosperm xylem structure with safety and efficiency. *Tree Physiology* **26**: 689–701.

Hacke UG, Sperry JS, Feild TS, Sano Y, Sikkema EH, Pittermann J. 2007. Water transport in vesselless angiosperms: conducting efficiency and cavitation safety. *International Journal of Plant Sciences* **168**: 1113–1126.

Herbette S, Bouchet B, Brunel N, Bonnin E, Cochard H, Guillon F. 2015. Immunolabelling of intervessel pits for polysaccharides and lignin helps in understanding their hydraulic properties in *Populus tremula* × *alba*. *Annals of Botany* **115**: 187–199.

Hillabrand RM, Hacke UG, Lieffers VJ. 2016. Drought-induced xylem pit membrane damage in aspen and balsam poplar. *Plant, Cell & Environment* **39**: 2210–2220.

Hölttä T, Vesala T, Perämäki M, Nikinmaa E. 2002. Relationships between embolism, stem water tension, and diameter changes. *Journal of Theoretical Biology* **215**: 23–38.

Jansen S, Choat B, Pletsers A. 2009. Morphological variation of intervessel pit membranes and implications to xylem function in angiosperms. *American Journal of Botany* **96**: 409–419.

Jansen S, Gortan E, Lens F, Gullo MAL, Salleo S, Scholz A, Stein A, Trifilò P, Nardini A. 2011. Do quantitative vessel and pit characters account for ion-mediated changes in the hydraulic conductance of angiosperm xylem? *New Phytologist* **189**: 218–228.

Jansen S, Klepsch M, Li S, Kotowska M, Schiele S, Zhang Y, Schenk H. 2018. Challenges in understanding air-seeding in angiosperm xylem. *Acta Horticulturae* **1222**: 13–20.

Jansen S, Pletsers A, Sano Y. 2008. The effect of preparation techniques on SEM-imaging of pit membranes. *IAWA Journal* **29**: 161–178.

Kaack L, Altaner CM, Carmesin C, Diaz A, Holler M, Kranz C, Neusser G, Odstrcil M, Schenk HJ, Schmidt V *et al.* 2019. Function and three-dimensional structure of intervessel pit membranes in angiosperms: a review. *International Association of Wood Anatomists Journal* **40**: 673–702.

Kanduč M, Schneck E, Loche P, Jansen S, Schenk HJ, Netz RR. 2020. Cavitation in lipid bilayers poses strict negative pressure stability limit in biological liquids. *Proceedings of the National Academy of Sciences, USA* **117**: 10733–10739.

Klepsch MM, Schmitt M, Paul JK, Jansen S. 2016. The chemical identity of intervessel pit membranes in *Acer* challenges hydrogel control of xylem hydraulic conductivity. *Annals of Botany PLANTS* **8**: 8:plw052.

Kotowska MM, Thom R, Zhang Y, Schenk HJ, Jansen S. 2020. Within-tree variability and sample storage effects of bordered pit membranes in xylem of *Acer pseudoplatanus*. *Trees* **34**: 61–71.

Law BM, McBride SP, Wang JY, Wi HS, Paneru G, Betelu S, Ushijima B, Takata Y, Flanders B, Bresme F *et al.* 2017. Line tension and its influence on droplets and particles at surfaces. *Progress in Surface Science* **92**: 1–39.

Lens F, Sperry JS, Christman MA, Choat B, Rabaey D, Jansen S. 2011. Testing hypotheses that link wood anatomy to cavitation resistance and hydraulic conductivity in the genus *Acer*. *New Phytologist* **190**: 709–723.

Levionnois S, Jansen S, Wandji RT, Beauchêne J, Ziegler C, Coste S, Stahl C, Delzon S, Authier L, Heuret P. 2021. Linking drought-induced xylem embolism resistance to wood anatomical traits in Neotropical trees. *New Phytologist* **229**: 1453–1466.

Li S, Feifel M, Karimi Z, Schuldt B, Choat B, Jansen S. 2016a. Leaf gas exchange performance and the lethal water potential of five European species during drought. *Tree Physiology* **36**: 179–192.

Li S, Lens F, Espino S, Karimi Z, Klepsch M, Schenk HJ, Schmitt M, Schuldt B, Jansen S. 2016b. Intervessel pit membrane thickness as a key determinants of embolism resistance in angiosperm xylem. *IAWA Journal* **37**: 152–171.

Li S, Wang J, Yin Y, Li X, Deng L, Jiang X, Chen Z, Li Y. 2020. Investigating effects of bordered pit membrane morphology and properties on plant xylem hydraulic functions — A case study from 3D reconstruction and microflow modelling of pit membranes in angiosperm xylem. *Plants* **9**: 231.

Loepfe L, Martinez-Vilalta J, Piñol J, Mencuccini M. 2007. The relevance of xylem network structure for plant hydraulic efficiency and safety. *Journal of Theoretical Biology* **247**: 788–803.

Mrad A, Domec J-C, Huang C-W, Lens F, Katul G. 2018. A network model links wood anatomy to xylem tissue hydraulic behaviour and vulnerability to cavitation. *Plant, Cell & Environment* **41**: 2718–2730.

Nardini A, Dimasi F, Klepsch M, Jansen S. 2012. Ion-mediated enhancement of xylem hydraulic conductivity in four *Acer* species: relationships with ecological and anatomical features. *Tree Physiology* **32**: 1434–1441.

O'Brien TP. 1970. Further observations on hydrolysis of the cell wall in the xylem. *Protoplasma* **69**: 1–14.

Oda Y, Fukuda H. 2013. Rho of plant GTPase signaling regulates the behavior of *Arabidopsis* Kinesin-13A to establish secondary cell wall patterns. *The Plant Cell* **25**: 4439–4450.

Park J, Go T, Ryu J, Lee SJ. 2019. Air spreading through wetted cellulose membranes: implications for the safety function of hydraulic valves in plants. *Physical Review E* **100**: 32409.

Pesacreta TC, Groom LH, Rials TG. 2005. Atomic force microscopy of the intervessel pit membrane in the stem of *Sapium sebiferum* (Euphorbiaceae). *IAWA Journal* **26**: 397–426.

Plavcová L, Hacke UG. 2012. Phenotypic and developmental plasticity of xylem in hybrid poplar saplings subjected to experimental drought, nitrogen fertilization, and shading. *Journal of Experimental Botany* **63**: 6481–6491.

Plavcová L, Jansen S, Klepsch M, Hacke UG. 2013. Nobody's perfect: can irregularities in pit structure influence vulnerability to cavitation? *Frontiers in Plant Science* **4**: 453.

Roth-Nebelsick A. 2019. It's contagious: calculation and analysis of xylem vulnerability to embolism by a mechanistic approach based on epidemic modeling. *Trees* **33**: 1519–1533.

Sanchez-Martinez P, Martínez-Vilalta J, Dexter KG, Segovia RA, Mencuccini M. 2020. Adaptation and coordinated evolution of plant hydraulic traits. *Ecology Letters* **23**: 1599–1610.

Sano Y. 2005. Inter- and intraspecific structural variations among intervascular pit membranes, as revealed by field-emission scanning electron microscopy. *American Journal of Botany* **92**: 1077–1084.

Satarifard V, Grafmüller A, Lipowsky R. 2018. Nanodroplets at membranes create tight-lipped membrane necks via negative line tension. *ACS Nano* **12**: 12424–12435.

Schenk, HJ, Espino, S, Rich-Cavazos, SM, Jansen, S. 2018. From the sap's perspective: The nature of vessel surfaces in angiosperm xylem. *American Journal of Botany* **105**: 172–185.

Schenk HJ, Espino S, Romo DM, Nima N, Do AYT, Michaud JM, Papahadjopoulos-Sternberg B, Yang J, Zuo YY, Steppe K *et al.* 2017. Xylem surfactants introduce a new element to the cohesion-tension theory. *Plant Physiology* **173**: 1177–1196.

Schenk HJ, Michaud JM, Mocko K, Espino S, Melendres T, Roth MR, Welti R, Kaack L, Jansen S. 2021. Lipids in xylem sap of woody plants across the angiosperm phylogeny. *The Plant Journal*. doi: 10.1111/tpj.15125.

Schenk HJ, Steppe K, Jansen S. 2015. Nanobubbles: a new paradigm for air-seeding in xylem. *Trends in Plant Science* **20**: 199–205.

Schmid R, Machado RD. 1968. Pit membranes in hardwoods—fine structure and development. *Protoplasma* **66**: 185–204.

Scholz A, Rabaey D, Stein A, Cochard H, Smets E, Jansen S. 2013. The evolution and function of vessel and pit characters with respect to cavitation resistance across 10 *Prunus* species. *Tree Physiology* **33**: 684–694.

Schuldt B, Buras A, Arend M, Vitasse Y, Beierkuhnlein C, Damm A, Gharun M, Grams TEE, Hauck M, Hajek P *et al.* 2020. A first assessment of the impact of the extreme 2018 summer drought on Central European forests. *Basic and Applied Ecology* **45**: 86–103.

Schuldt B, Knutzen F, Delzon S, Jansen S, Müller-Haubold H, Burlett R, Clough Y, Leuschner C. 2016. How adaptable is the hydraulic system of European beech in the face of climate change-related precipitation reduction? *New Phytologist* **210**: 443–458.

Shane MW, McCully ME, Canny MJ. 2000. Architecture of branch-root junctions in maize: structure of the connecting xylem and the porosity of pit membranes. *Annals of Botany* **85**: 613–624.

Sorek Y, Greenstein S, Netzer Y, Shtein I, Jansen S, Hochberg U. 2021. An increase in xylem embolism resistance of grapevine leaves during the growing season is coordinated with stomatal regulation, turgor loss point and intervessel pit membranes. *New Phytologist* **229**: 1955–1969.

Sperry JS, Hacke UG. 2004. Analysis of circular bordered pit function I. Angiosperm vessels with homogenous pit membranes. *American Journal of Botany* **91**: 369–385.

Sperry JS, Hacke UG, Pittermann J. 2006. Size and function in conifer tracheids and angiosperm vessels. *American Journal of Botany* **93**: 1490–1500.

Sugiyama Y, Nagashima Y, Wakazaki M, Sato M, Toyooka K, Fukuda H, Oda Y. 2019. A Rho-actin signaling pathway shapes cell wall boundaries in Arabidopsis xylem vessels. *Nature Communications* **10**: 468.

Sugiyama Y, Wakazaki M, Toyooka K, Fukuda H, Oda Y. 2017. A novel plasma membrane-anchored protein regulates xylem cell-wall deposition through microtubule-dependent lateral inhibition of Rho GTPase domains. *Current Biology* **27**: 2522–2528.

Thonglim A, Delzon S, Larter M, Karami O, Rahimi A, Offringa R, Keurentjes JJB, Balazadeh S, Smets E, Lens F. 2020. Intervessel pit membrane thickness best explains variation in embolism resistance amongst stems of Arabidopsis thaliana accessions. *Annals of Botany*. doi: 10.1093/aob/mcaa196.

Tixier A, Herbette S, Jansen S, Capron M, Tordjeman P, Cochard H, Badel E. 2014. Modelling the mechanical behaviour of pit membranes in bordered pits with respect to cavitation resistance in angiosperms. *Annals of Botany* **114**: 325–334.

Torres-Ruiz JM, Cochard H, Choat B, Jansen S, López R, Tomášková I, Padilla-Díaz CM, Badel E, Burlett R, King A *et al.* 2017. Xylem resistance to embolism: presenting a simple diagnostic test for the open vessel artefact. *New Phytologist* **215**: 489–499.

Trueba S, Delzon S, Isnard S, Lens F. 2019. Similar hydraulic efficiency and safety across vesselless angiosperms and vessel-bearing species with scalariform perforation plates. *Journal of Experimental Botany* **70**: 3227–3240.

Vilagrosa A, Cortina J, Gil-Pelegrín E, Bellot J. 2003. Suitability of drought-preconditioning techniques in mediterranean climate. *Restoration Ecology* **11**: 208–216.

Wason JW, Anstreicher KS, Stephansky N, Huggett BA, Brodersen CR. 2018. Hydraulic safety margins and air-seeding thresholds in roots, trunks, branches and petioles of four northern hardwood trees. *New Phytologist* **219**: 77–88.

Wheeler JK, Huggett BA, Tofte AN, Rockwell FE, Holbrook NM. 2013. Cutting xylem under tension or supersaturated with gas can generate PLC and the appearance of rapid recovery from embolism. *Plant, Cell & Environment* **36**: 1938–1949.

Wheeler JK, Sperry JS, Hacke UG, Hoang N. 2005. Inter-vessel pitting and cavitation in woody Rosaceae and other vesselled plants: a basis for a safety versus efficiency trade-off in xylem transport. *Plant, Cell & Environment* **28**: 800–812.

Yang J, Michaud MJ, Jansen S, Schenk HJ, Zuo YY. 2020. Dynamic surface tension of xylem sap lipids. *Tree Physiology* **40**: 433–444.

Zhang H, Zhao C, Li Z, Li J. 2016. The fiber charge measurement depending on the poly-DADMAC accessibility to cellulose fibers. *Cellulose* **23**: 163–173.

Zhang Y, Carmesin C, Kaack L, Klepsch MM, Kotowska M, Matei T, Schenk HJ, Weber M, Walther P, Schmidt V *et al.* 2020. High porosity with tiny pore constrictions and unbending pathways characterize the 3D structure of intervessel pit membranes in angiosperm xylem. *Plant, Cell & Environment* **43**: 116–130.

Zhang Y, Klepsch M, Jansen S. 2017. Bordered pits in xylem of vesselless angiosperms and their possible misinterpretation as perforation plates. *Plant, Cell & Environment* **40**: 2133–2146.

Zimmermann MH. 1983. *Xylem structure and the ascent of sap*. New York, NY, USA: Springer-Verlag.

Supporting Information

Additional Supporting Information may be found online in the Supporting Information section at the end of the article.

Fig. S1 Frequency distribution of the number of intervessel pits for a vessel with average dimensions and pit characteristics.

Fig. S2 Transmission electron microscopy (TEM) images of intervessel pit membranes of different thickness.

Fig. S3 Results of Model 1, Scenario 2; relationship between T_{PM} and the size of a pore constriction.

Fig. S4 Modelled embolism propagation pressure based on Model 1, with a surface tension of 72 mN m^{-1}.

Fig. S5 Three-dimensional graph based on Scenario 2 of Model 2, with a 0.5 probability of having a large pore in a single pit membrane layer.

Fig. S6 Two-dimensional graph based on Model 2 showing the probability of a large pore in a vessel of up to 400 000 pits per vessel.

Methods S1 Detailed model descriptions.

Methods S2 Model 1, Microsoft Excel function.

Methods S3 R script for Model 3.

Methods S4 Protocols: plant material, xylem embolism resistance, TEM, vessel and pit characteristics.

Methods S5 Equations for the relationship between T_{PM} and embolism propagation pressure used in Model 1.

Table S1 Dataset of the 31 angiosperm species studied, with reference to the anatomical and hydraulic traits measured.

Please note: Wiley Blackwell are not responsible for the content or functionality of any Supporting Information supplied by the authors. Any queries (other than missing material) should be directed to the *New Phytologist* Central Office.